crystals

MDPI

Communication

Preparation of NbAs Single Crystal by the Seed Growth Process

Yinchang Sun †, Bojin Zhao †, Zongju Huo, Hongjun Liu, Yongkuan Xu, Zhanggui Hu and Hailong Qiu *

Tianjin Key Laboratory of Functional Crystal Materials, Institute of Functional Crystal, Tianjin University of Technology, Tianjin 300384, China; acencore@163.com (Y.S.); zbojin@stud.tjut.edu.cn (B.Z.); huozongju@stud.tjut.edu.cn (Z.H.); hjliu@email.tjut.edu.cn (H.L.); orientallion@126.com (Y.X.); hu@tjut.edu.cn (Z.H.)

* Correspondence: qiu@tjut.edu.cn

† The authors contribute equally to this work.

Abstract: A Weyl semimetal is a novel crystal with low-energy electronic excitations that behave as Weyl fermions. It has received worldwide interest and was believed to have introduced the next era of condensed matter physics after graphene and three-dimensional topological insulators. However, it is not easy to obtain a single large-sized crystal because there are many nucleations in the preparation process. A bottom-seed CVT growth method is proposed in this paper, and we acquired the large-sized, high-quality NbAs single crystals up to $4 \times 3 \times 3$ mm^3 finally. X-ray diffraction and STEM confirmed that they are tetragonal NbAs, which the key is to using the seed crystal in a vertical growth furnace. Notably, the photoelectric properties of the crystal are obtained under the existing conditions, which paves the way for follow-up work.

Keywords: Weyl semimetal; NbAs single crystal; seed growth; photoelectric

Citation: Sun, Y.; Zhao, B.; Huo, Z.; Liu, H.; Xu, Y.; Hu, Z.; Qiu, H. Preparation of NbAs Single Crystal by the Seed Growth Process. *Crystals* **2022**, *12*, 249. https://doi.org/10.3390/cryst12020249

Academic Editors: Chunhui Yang, Ning Ye and Haohai Yu

Received: 19 January 2022
Accepted: 9 February 2022
Published: 11 February 2022

1. Introduction

Weyl semimetals (WSMs) have obvious chiral fermions and spin structures that can cause a novel carrier response under pulsed laser excitation, leading to new optical phenomena [1–5]. Because of these characteristics, WSMs have been favored by many scientists in recent years. Furthermore, according to the photodetection theory, semiconductors, which have bandgaps smaller than the photo energy of incident light [6], can have their electrons excited from valance bands to conduction bands to achieve a photoresponse. Therefore, WSM materials have excellent development potential in designing and applying new devices [7–9]. NbAs is a typical WSM.

NbAs is one of the first-class Weyl semimetals (TaAs, TaP, NbAs, NbP), which crystallizes in a body-centered tetragonal unit cell with lattice constants a = 3.452 Å, c = 11.679 Å, and the space group is $I4_1md(C_{4v}^{11})$ [10,11] (as shown in Figure 1a). For NbAs, the melting point of Nb reaches 2468 °C, while the As (melting point: 817 °C) has the characteristics of direct sublimation without liquefaction when heated to 613 °C under pressure. Therefore, a high-pressure environment is very favorable for the reaction conditions of As [12]. At the same time, regarding NbAs, as a compound containing As, for safety reasons, the open growth system cannot meet the requirements of the growth environment. Besides NbAs, other phases, such as $NbAs_2$, Nb_3As, Nb_4As_3, exist in the Nb-As binary system. Therefore, in reports, the chemical vapor transport (CVT) method is usually used to grow large-sized, high-quality NbAs single crystals [13].

Unfortunately, there are always many nucleations in this process during the growth of NbAs. We believe that there are two reasons for this. On the one hand, the transmission capacity of the raw material atmosphere is limited. On the other hand, the quartz tube's axial and radial temperature gradients are large [14,15]. As a result, the environment of the raw material atmosphere during crystal growth is uneven and unstable, and the continuity of crystal growth cannot be maintained. Finally, small polycrystalline grains are obtained,

which is very unfavorable to the growth of large-sized crystals. This paper provides a bottom-seed crystal growth process, which solves the above problems. Firstly, the vertical CVT process growth method is used; the raw materials are placed at the bottom of the quartz tube [16]. In this case, the raw material concentration at the bottom of the quartz tube will be much greater than that at the top, which is conducive to the growth of crystals at the bottom of the quartz tube when the transport distance of gas is significantly shortened. Secondly, the volume of the growth zone used for vertical growth will be much smaller than that of the horizontal CVT method, thus reducing the axial and radial temperature gradients in the growth zone and further ensuring the stability and continuity of crystal growth. In addition, the crystal with the exposed surface of (001) is added as the seed crystal, which provides a growth site for the raw material atmosphere and reduces the barrier of crystal growth. Thus, we believe that these methods are the key to obtaining large-sized and high-quality crystals [17,18].

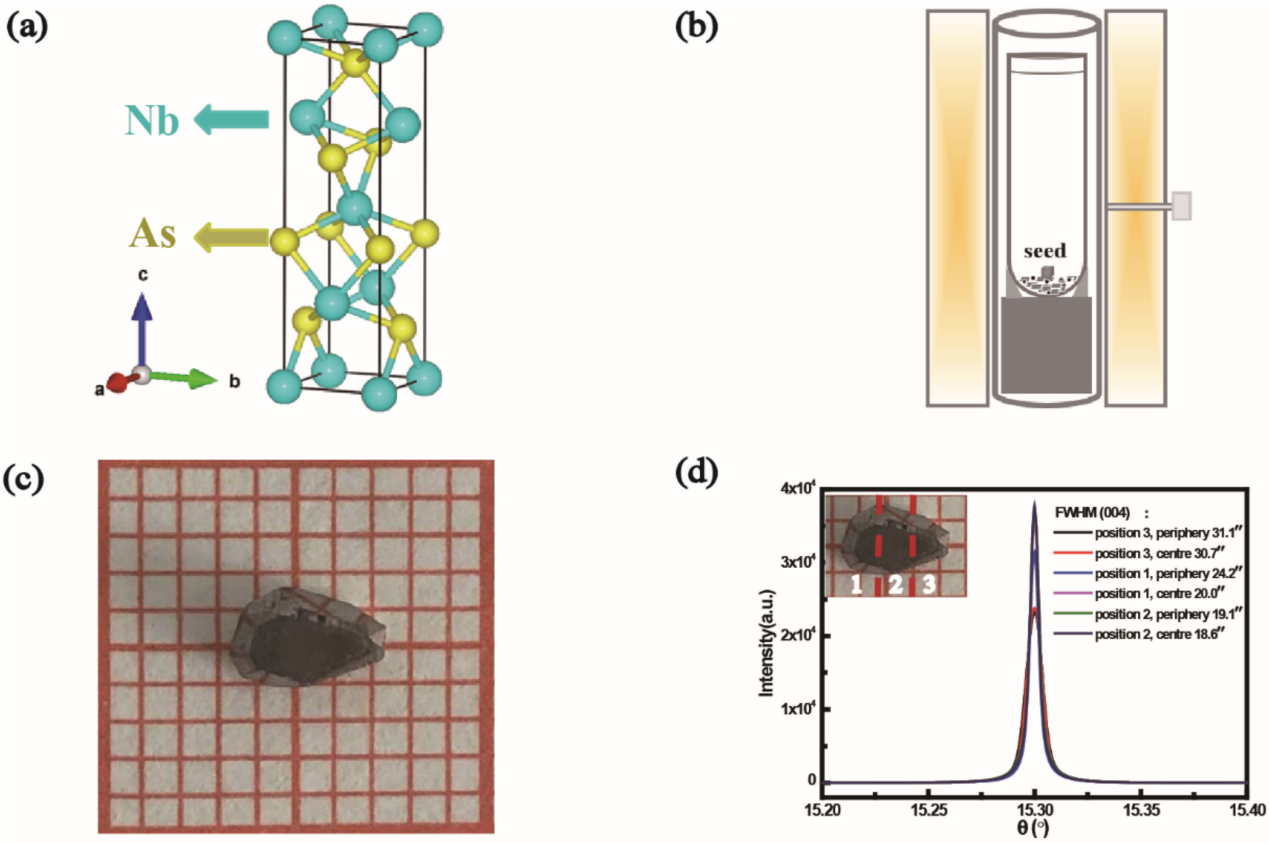

Figure 1. (**a**) Crystal structure of NbAs. (**b**) Schemes of the chemical vapor transport experiments for crystallization of NbAs in a two-step method. (**c**) Photograph of NbAs single crystal. (**d**) X-ray rocking curves of the three different regions (as shown in the illustration) for (004) face show good crystallinity with Full Width at Half Maxima (FWHM) less than 31.1″.

2. Materials and Methods

2.1. Synthesis of NbAs Crystal

As is well known, exploring an appropriate growth process is the key to obtaining large crystals. We report a bottom-seed CVT growth method in this work, and Figure 1b shows the experimental configurations. In a typical run, Nb foil (99.99%), As (99.99%), and I_2 (99.99%) with the molar ratio of 1:1.05:0.05 were selected as raw materials, loaded in a 45 mL quartz tube, which was 14 cm in length and 2 cm in inner diameter. Meanwhile, we selected the grain of NbAs with a classy crystal orientation (here, the {001} facets were selected as the growth section) as the seed; then, it was added into the quartz tube together with the raw materials.

The quartz tube was initially filled with argon and sealed quickly to avoid the loss of iodine and arsenic when evacuated to a pressure below 4×10^{-4} Pa. Nb powder and Nb foil have a larger specific surface area and few defects, which is conducive to acquiring large crystals [11]. In addition, Saini et al. [19] found that As must be excessive if we wish to obtain the best crystal growth effect, even for the growth of metal-rich crystals in the study of the Pd-As system. Therefore, here, we added a slight excess of As to achieve the growth of the NbAs single crystal. As for I_2, it plays a catalytic and transport role according to the kinetic analysis of I_2 in the growth of a TaAs crystal by Li [12] et al. Moreover, to avoid the explosion of the quartz tube caused by the vapor pressure generated when I_2 and As are sublimated to a gaseous form, the amount of I_2 selected was 1 mg/ml here.

Afterward, the quartz tube was heated gradually from room temperature to 1000 °C over 72 h, kept for 30 days in a high-temperature environment at 1050 °C, and finally naturally cooled down to room temperature (although the reaction time is longer, after comparing the growth results many times, a long-term heat preservation process was found to be essential). Through the above work, we obtained NbAs single crystals with good crystallinity, with a size of up to $4 \times 3 \times 3$ mm^3 in three dimensions (as Figure 1c shows). However, we have not seen a giant NbAs single-crystal reported to date. In addition, the X-ray rocking curves (Figure 1d) showed that the full widths at half maximum (FWHM) were less than 31.1" for the three different regions (as shown in the illustration) for the (004) face, suggesting the high quality of the grown crystals in terms of crystallinity.

2.2. Device Fabrication

NbAs devices are produced by dry transfer technology under argon filling conditions. The NbAs crystal size is close to 2 mm × 1.5 mm × 1.5 mm cubed (length × width × height). Since the sample size was relatively small, we did not choose the spin coating Ag adhesive method. We chose to attach the tape to the (001) plane of the NbAs crystal (the parameters of the sample crystal plane were determined by XRD) and left blank boundaries on both sides. Then, the sample surface was fully evaporated by evaporation. At the end of the evaporation, the tape attached to the surface was carefully torn apart so that the tape attached to the sample surface became the rectangular channel of the device. Both sides were conductive electrodes: Cr/Au (10 nm/70 nm). The reason for choosing a Cr/Au electrode is that the stability of the Cr/Au electrode material deposited by evaporation is relatively good. In addition, the Cr/Au evaporation deposition electrode can overcome the possible problems of poor contact and unstable conductivity of the Ag and Cu conductive adhesive spin coating. Finally, the prototype image of the NbAs photodetector is shown in Figure 2.

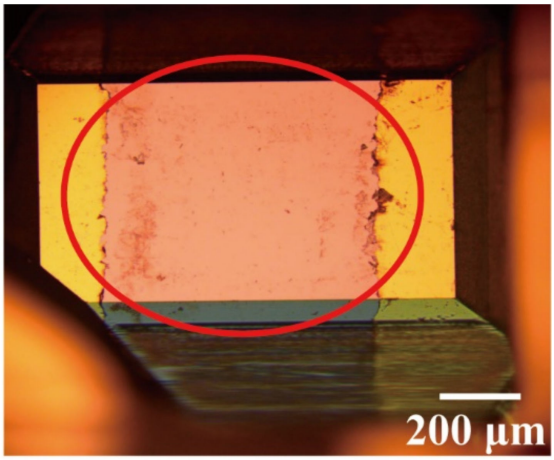

Figure 2. Device pictures of NbAs photodetectors.

Semiconductor Parameter Analyzer (Keithley-4200-SCS, Bradford, UK) and standard probe station are earmarks of electronic and photoelectric measurement. The photoresponse of the device was measured using a laser with adjustable power and incident wavelength.

Powder X-ray Diffraction (PXRD). The PXRD measurements were collected using a SmartLab3KW X-ray diffractometer (Rigaku, Tokyo, Japan) at room temperature (Cu Kα radiation). All the data were collected in the 2θ range of 20−70° with a step size of 0.01° and a step time of 2 s.

Raman Spectroscopy. The Raman spectra were collected from the single crystals of NbAs on a confocal microscope laser Raman spectrometer (WITec, Munich, Germany) equipped with a CCD detector using 532 nm radiation. The Raman data collection was accomplished in 20 s.

X-Ray Photoelectron Spectroscopy (XPS). The XPS was performed on a Thermo Scientific (Waltham, MA, US) device, ESCALAB250Xi, with a monochromatic Al X-ray source. The power was 150 W, and the spot size was 300 micrometers.

Scanning Transmission Electron Microscopy (STEM). The sample was prepared using the standard polymer transfer method. STEM images and HAASF-STEM were obtained using FEI, TECNAI G2Spirit TWIN (Thermo Scientific Waltham, MA, US).

Energy Dispersive X-ray Spectroscopy (EDX). Microprobe elemental analyses and the elemental distribution map were performed using an energy-dispersive X-ray spectroscope (EDX) scanning transmission electron microscopy (Thermo Scientific Waltham, MA, US). The average atomic ratio in NbAs was Nb: As = 49.72: 50.28, which was approximately equal to the theoretical one, 1:1.

3. Results and Discussion

3.1. Structure Analysis

Niobium arsenide, NbAs, crystallizes in a body-centered tetragonal Bravai lattice, space group $I4_1md$, point group C_{4v}. Our X-ray diffraction (XRD) obtained lattice constants of a = 3.45 Å and c = 11.68 Å, consistent with earlier crystallographic studies. In Figure 3a, the upper black line in the diagram indicates the XRD of NbAs powder (obtained by grinding NbAs crystals), which is completely consistent with the data in PDF No. 17-0896 (blue line in the figure). In addition, we checked the main peak positions and marked the corresponding crystal planes. Among them, a few noncorresponding crystal planes belonged to polyarsenides, marked with the yellow graphic (such as $NbAs_2$) [20–22], and their existence is temporarily unavoidable in the growth of this type of crystal. The result shows that the grown NbAs crystals have high purity and few miscellaneous items.

Note that, for the seed of NbAs, its exposed surface is mainly {001} facets, and the one-dimensional length is approximately 1.5 mm. These faces have a relatively larger lattice plane space and, therefore, a slower growth rate and thus are found more frequently than others in the as-grown crystals [12]. Nevertheless, when we use these seed crystals for further growth, they can provide a basis for the growth of other planes in the NbAs crystal so that other poorly developed planes can be displayed.

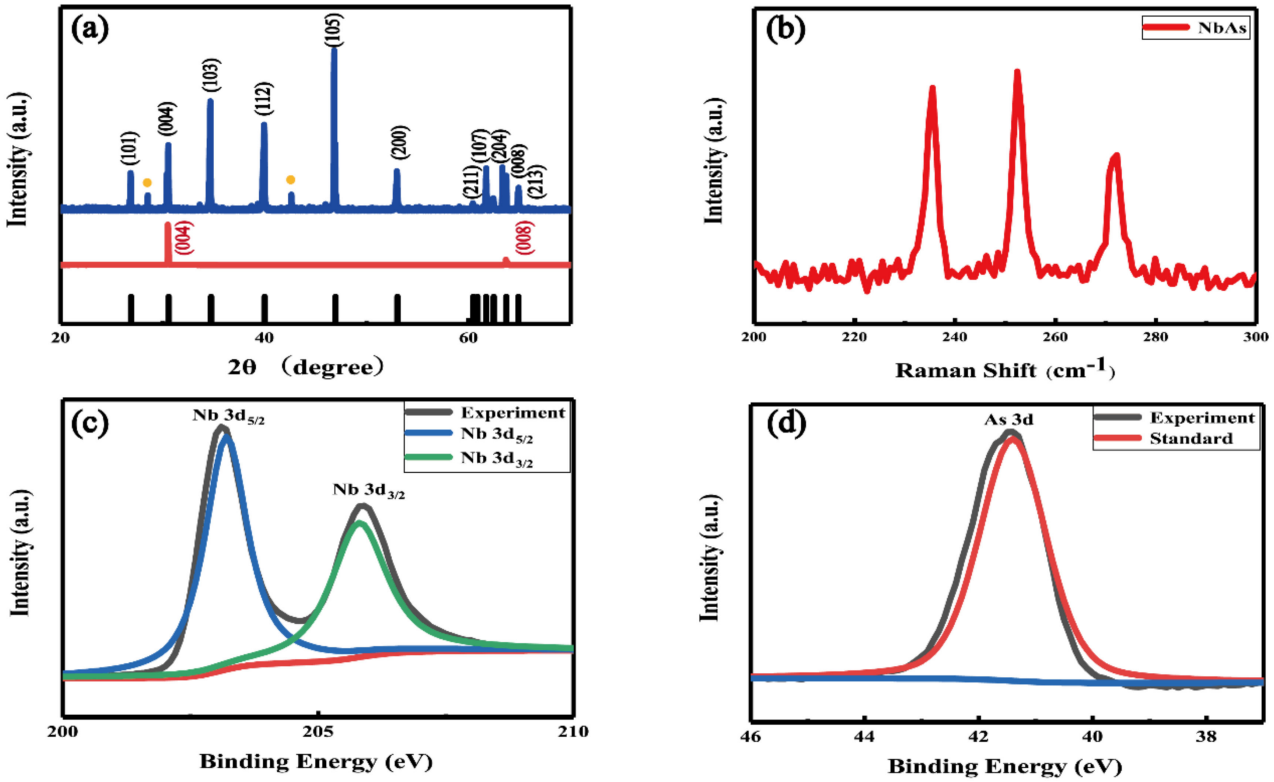

Figure 3. (**a**) XRD pattern of NbAs crystal powder. The {001} facets of NbAs single crystal (black line in the figure is PDF card of the NbAs and diffraction peaks of the polyarsenides marked by yellow dots). (**b**) Raman spectra of NbAs single crystal. (**c**,**d**) Typical XPS spectrum of Nb 3d and As 3d core level of NbAs single crystal.

3.2. Material Characterization

As a widely used and powerful characterization method, Raman spectroscopy can preliminarily elucidate the phono information of synthetic crystals [23]. We characterized the NbAs crystals by Raman spectroscopy, shown in Figure 3b for the bulk NbAs crystals, which mainly displayed three prominent Raman peaks in the range of 180–330 cm^{-1}. According to the previous Raman spectra of NbAs [24,25], we marked the vibration modes corresponding to the three peak positions in Figure 3b, which are B_1 mode at 234 cm^{-1}, B_1 mode at 252 cm^{-1}, and A_1 mode at 272 cm^{-1}, respectively. The spectral characterization results are consistent with the theoretical data [3,26], indicating the excellent crystalline quality of the NbAs crystals.

A typical X-ray photoelectron spectroscopy (XPS) spectrum of NbAs is shown in Figure 3c,d. The XRD data show that there may have been a small amount of polyarsenide in the sample. Therefore, we first etched the sample in the XPS test and obtained the XPS of NbAs after removing the surface layer of 20 nm. Then, the experimental data were labeled by consulting the literature and comparing the database, i.e., Nb $3d_{5/2}$ at 203.1 eV and Nb $3d_{3/2}$ at 205.8 eV. The pair had energy splitting of ~2.7 eV [26], which is consistent with our expectation for the spin–orbit-split $3d_{5/2}$ and $3d_{3/2}$ levels of Nb core levels. Similarly, the XPS data of As at the low binding energy end are consistent with the reported data, indicating that 41.5 eV belongs to the 3d orbit of As. Again, these are consistent with the XPS results of NbAs materials reported.

As a means of characterizing crystal quality and structure, atomic morphology characterization can more intuitively and accurately reflect the specific information of Nb and As atoms in NbAs crystals. Figure 4a is a typical STEM image that shows clear lattice stripes, and Figure 4b is a low-power SEM image of bulk NbAs placed on an ultra-thin carbon film. The test results indicate that the spacing between (001) and (010) is approximately 3.4 Å, which is consistent with the data in the literature. The diffraction points of (110) and

(001) are also shown in the Fast Fourier Transform (FFT) diagram in Figure 4a. Similarly, the structure of these facets is shown in Figure 4d,e. In recent research on NbAs crystals, the coexistence of hexagonal and tetragonal phases was discussed. The observation or characterization of a NbAs single crystal on the atomic scale shows that the crystal is a single-phase structure [10].

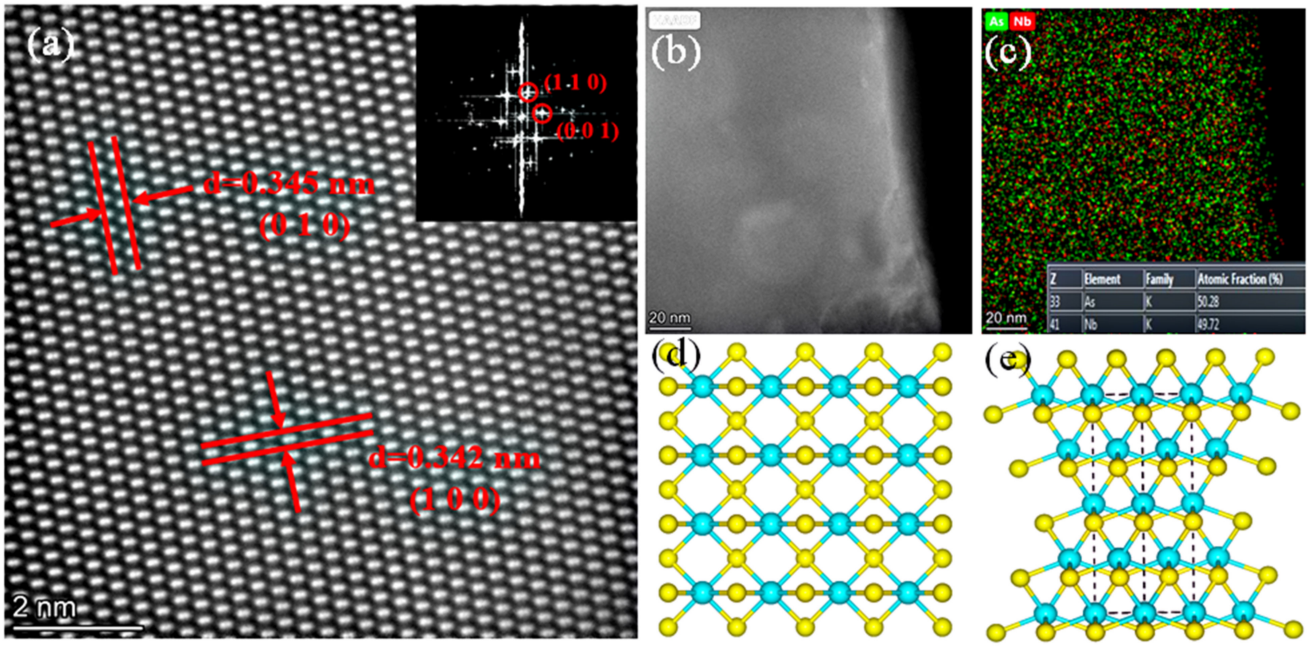

Figure 4. (**a**) HAASF-STEM images of NbAs single crystal (the illustration is FFT pattern). (**b**) TEM images of bulk NbAs placed on an ultra-thin carbon film. (**c**) EDX mapping of bulk NbAs. (**d**) and (**e**) show the (001) and (110) facets of NbAs single crystal.

In our experiments, the coexistence phase problem was overcome by improving the bottom-seed method and synthesizing the high-quality NbAs crystals with a single-phase structure, highlighting our work's significance. The EDX is shown in Figure 4c, in which the uniform distribution of Nb and As atoms can be seen. The illustration also indicates that Nb:As is close to 1:1. This information proves the high quality of our crystals on the micro-scale.

3.3. Photoelectric Response Detection of NbAs Crystal

As for the photoelectric response of NbAs, due to the inherent limitations of the experimental environment, we only investigated the photoelectric detection prototype of Weyl semimetal NbAs in the visible region (550–800 nm) at room temperature.

After evaporation, the tape was carefully torn off, and the area covered by the tape became the device channel of the unevaporated electrode. A schematic diagram of the NbAs photodetector is shown in Figure 5a. The illustration in Figure 5a shows the schematic diagram of the photoelectron generation principle of NbAs under light conditions. Under laser irradiation, NbAs absorbs photons and then causes electron transition to generate carriers, resulting in a photocurrent. With the opening and closing of the incident laser, the current difference between the light condition and the dark condition can be collected. The dark current (I_{dark}) is measured under the conditions of V_{DS} = −0.1 to 0.1 V and V_{GS} = 0 V. The I–V curve is shown in Figure 5b; the linearity of the curve indicates that the Schottky barrier at the contact interface between the NbAs sample and the Cr/Au electrode is shallow. Figure 5b illustrates an I–V output curve near 0 V and 0 mA. As can be seen, when V_{DS} = 0 V, the output curve does not entirely intersect with the X-axis (V_{DS} = 0V, $I_{DS} \approx -0.1$ mA). Therefore, we believe that the smoothness of the curve is poor and the actual measured current results at V_{DS} = 0 V are within the reasonable error range, and the

error is related to the electrode fabrication process, possible surface oxidation, and possible surface thermal effect. The incident light is usually projected on the (001) surface, as shown in the area marked by the red circle in Figure 2.

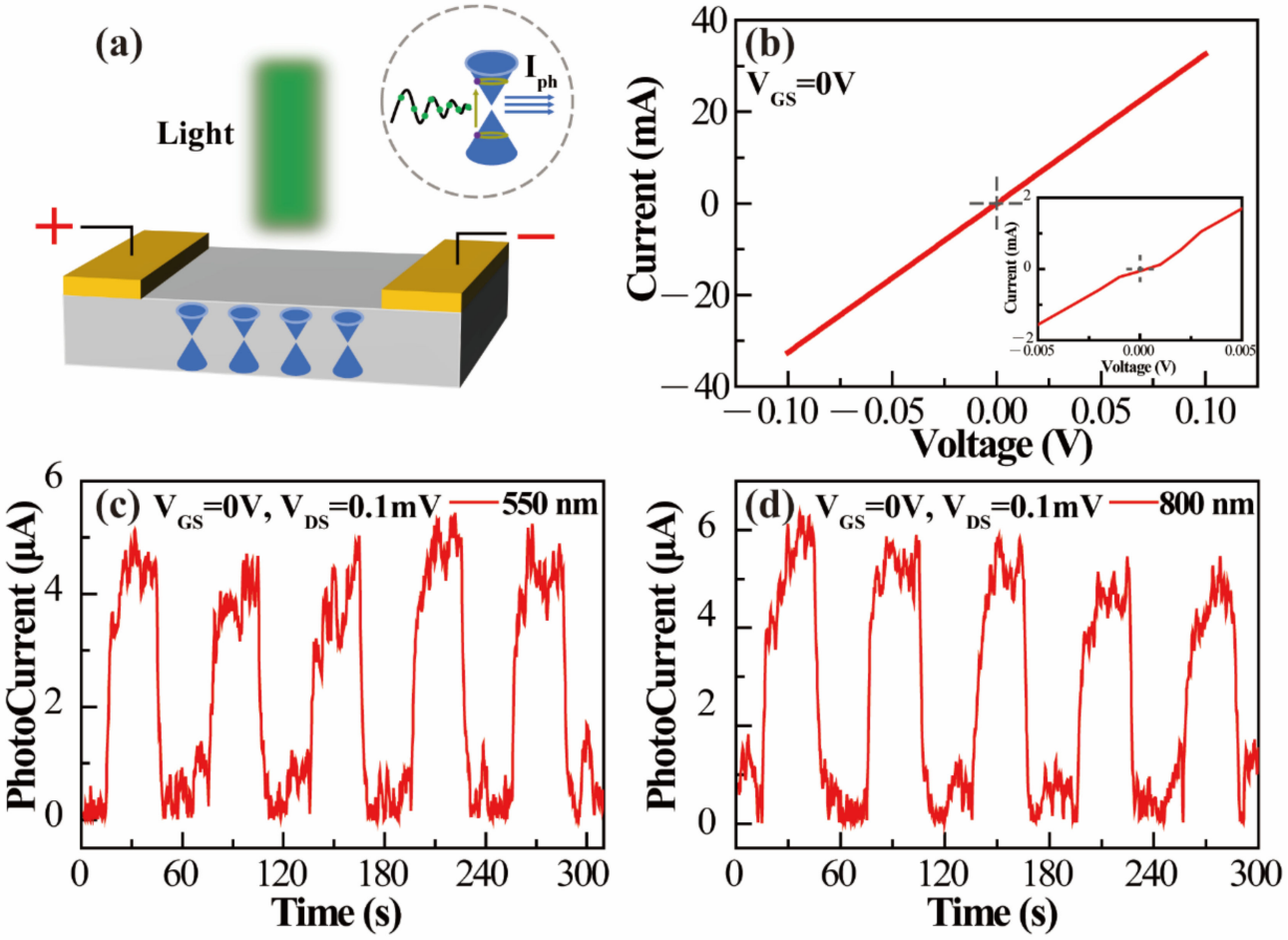

Figure 5. (**a**) Schematic diagram of NbAs photoelectric device equipment. Illustration: schematic diagram of photocurrent generation under illumination conditions. (**b**) The I–V curve of the photodetecting prototype. (**c**,**d**) When the V_{DS} = 0.1 mV, V_{GS} = 0 V, and the incident light intensity is 10 mW, the I–T curve of the device at 550 nm and 800 nm incident light is as shown.

The time-resolved photoelectric response curve of NbAs was measured at the source–drain voltage V_{DS} = 0.1 mV and gate voltage V_{GS} = 0 V. We only list the test results under 550 nm and 800 nm lasers, as shown in Figure 5c,d. It can be seen from the time-resolved I–T curve of NbAs that, under laser conditions, NbAs exhibits a μA-level light response current. Under light and dark conditions, different current outputs show the sensitivity of NbAs to the laser. In addition, the periodic fast switching of the bright current and dark current at room temperature indicates that NbAs has a strong absorption capacity for photons under laser irradiation. This process highlights the strong photon absorption of NbAs crystals in the visible region and at room temperature, indicating the advantages of NbAs in the field of photoelectric detection. By comparison, the light–dark current switching ratio is close to 5, but the light–dark current is relatively poor under stable conditions. Therefore, we believe that the electrode fabrication method may affect the test results. In addition, the laser has poor stability at 10 mW (if the laser intensity is too low, the photoresponse current of μA magnitude will be more difficult to distinguish) and cannot achieve a stable, high-intensity laser output, and this may cause the instability of the photoresponse current.

Although stable test conditions cannot be achieved, the photoelectric response current of more than μA magnitude only at 0.1 mV indicates the research potential of NbAs in photoelectric response detection [6,27,28].

The photoelectric responsivity (R) and detection rate (D^*) can be defined as follows [28–32]:

$$R = \frac{I_{ph}}{PA} \tag{1}$$

Among them, I_{ph}, P, and A represent the photocurrent, incident optical power density, and the effective irradiation area of the detector.

$$D^* = R\sqrt{\frac{S}{2qI_{dark}}} \tag{2}$$

where, R, S, q, and I_{dark} represent the responsivity, the effective irradiation area of the heterojunction, the primary charge, and the dark current, respectively. Figure 6a,b list the device's R and D^* related information in the range of 550–800 nm (corresponding to the incident photon energy of 1.5 to 2.25 eV) when the incident power is fixed at 10 mW. It can be seen that R and D* do not change significantly with the incident photon energy. Except for the high responsivity at 550 nm, the responsivity is stable at 2 mA/W (D^* close to 10^7 Jones). When the incident laser wavelength is 550 nm, R and D^* reach 16 mA/W and 1.1 × 10^8 Jones, respectively. This result provides clues as to the light response mechanism. It shows that NbAs has stronger absorption and more energy scattering events at short wavelengths, which helps to achieve a more significant light response. In addition, significantly more energy is transferred from the absorbed photons to the electrons excited on the short-wavelength side.

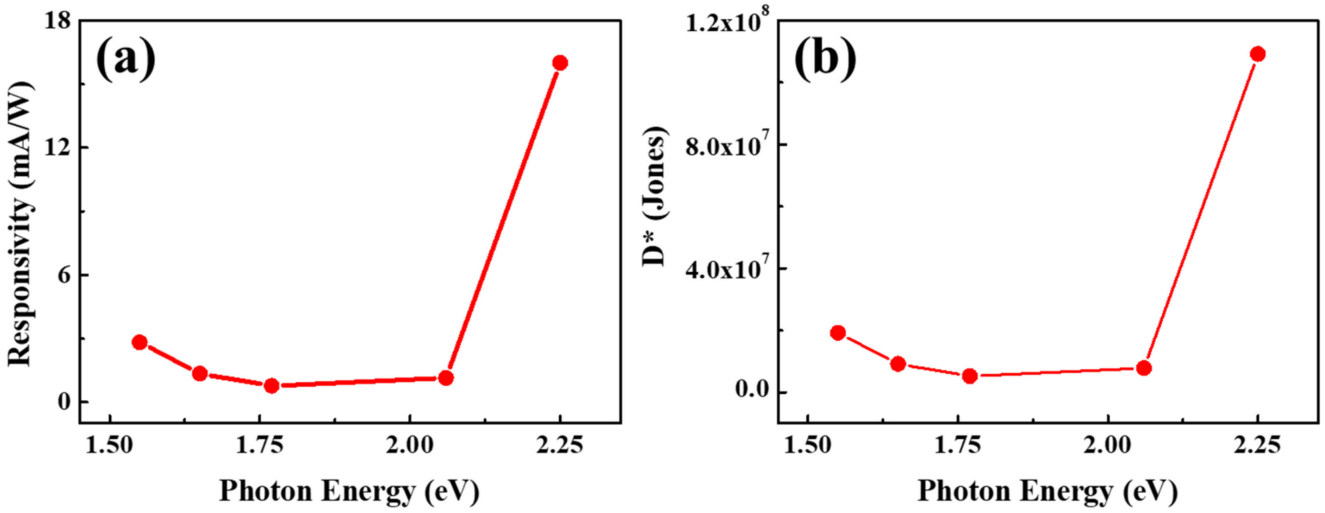

Figure 6. (**a**) Responsivity variation characteristics of NbAs photoelectric device prototype within 1.5 to 2.25 eV. (**b**) The relationship between the detection rate D^* of NbAs devices and the energy of incident photons.

It is worth noting that, according to reports [6], TaAs has a broad-spectrum light response from the visible range to the long-infrared range at room temperature. As for NbAs, we only conducted preliminary tests on its light response in the visible light range, and its broadband light response at room temperature still needs more in-depth theoretical and experimental research.

4. Conclusions

In summary, the one-dimensional size of the NbAs single crystal grown by the CVT method using the bottom-seed method can reach 4 mm, and the three-dimensional size can

reach $4 \times 3 \times 3$ mm^3. The quality of the product has been confirmed by powder XRD and Raman methods. More importantly, the atomic-level morphology characterization results show that we have overcome the multi-phase coexistence in the past growth process. XPS data explain that the surface state of NbAs crystals will be affected by oxygen and lead to some changes, as specific results need to be further studied and discussed. In addition, we prepared a prototype of the NbAs photodetector in the visible light range and discussed the relationship between R and D^* with the energy of incident photons. Our improved growth method provides a reference and helps in the growth of difficult-to-synthesize materials such as Weyl semimetal. At the same time, the synthesis of high-quality crystals guarantees the subsequent electrical properties research and photoelectric performance detection of this type of Weyl semimetal. Due to the inherent limitations of the experimental conditions, we only obtained the relevant information of the time-resolved response of the NbAs photodetector in the visible range and discussed the relationship between R, D^*, and the incident photon energy. By comparison, it was found that the test results of NbAs were similar to those of TaAs photodetectors in the visible range. In addition, the photoresponse current at μA level at room temperature indicated that NbAs has a reasonable photon absorption rate. In this experiment, we only fabricated a relatively primary NbAs optoelectronic device. With the help of the strong interaction between NbAs and light, the optimization design of the device will further improve the light response and then highlight the light response advantages of the Weyl semimetal in a wide range at room temperature. Excellent photon absorption and ambient temperature at room temperature indicate the potential of the Weyl semimetal in photoelectric detection.

Author Contributions: Methodology, Y.S.; validation, B.Z., Y.S., Y.X. and Z.H. (Zongju Huo); investigation, B.Z.; data curation, Y.S.; writing—original draft preparation, H.Q.; writing—review and editing, H.L.; project administration, Z.H. (Zhanggui Hu). All authors have read and agreed to the published version of the manuscript.

Funding: This research was funded by the NSFC (51972229, 51802218, 51872198, 52172151), the Natural Science Foundation of Tianjin (19JCYBJC17800), and the National Defense Science and Technology 173 Program (2021-JCJQ-JJ-0639).

Institutional Review Board Statement: Not applicable.

Informed Consent Statement: Not applicable.

Data Availability Statement: Not applicable.

Acknowledgments: The authors thank Wen Cheng Ma and Lu Jie Li for the technical support.

Conflicts of Interest: The authors declare that they have no conflicts of interest.

References

1. Xu, S.-Y.; Alidoust, N.; Belopolski, I.; Yuan, Z.; Bian, G.; Chang, T.-R.; Zheng, H.; Strocov, V.N.; Sanchez, D.S.; Chang, G.; et al. Discovery of a Weyl fermion state with Fermi arcs in niobium arsenide. *Nat. Phys.* **2015**, *11*, 748–754. [CrossRef]
2. Huang, S.M.; Xu, S.Y.; Belopolski, I.; Lee, C.C.; Chang, G.; Chang, T.R.; Wang, B.; Alidoust, N.; Bian, G.; Neupane, M.; et al. New type of Weyl semimetal with quadratic double Weyl fermions. *Proc. Natl. Acad. Sci. USA* **2016**, *113*, 1180–1185. [CrossRef] [PubMed]
3. Yuan, X.; Zhang, C.; Zhang, Y.; Yan, Z.; Lyu, T.; Zhang, M.; Li, Z.; Song, C.; Zhao, M.; Leng, P.; et al. The discovery of dynamic chiral anomaly in a Weyl semimetal NbAs. *Nat. Commun.* **2020**, *11*, 1259. [CrossRef] [PubMed]
4. Xu, Q.; Zhang, Y.; Koepernik, K.; Shi, W.; Van den Brink, J.; Felser, C.; Sun, Y. Comprehensive scan for nonmagnetic Weyl semimetals with nonlinear optical response. *Npj Comput. Mater.* **2020**, *6*, 1–7. [CrossRef]
5. Ji, Z.; Liu, G.; Addison, Z.; Liu, W.; Yu, P.; Gao, H.; Liu, Z.; Rappe, A.M.; Kane, C.L.; Mele, E.J.; et al. Spatially dispersive circular photogalvanic effect in a Weyl semimetal. *Nat. Mater.* **2019**, *18*, 955–962. [CrossRef]
6. Chi, S.; Li, Z.; Xie, Y.; Zhao, Y.; Wang, Z.; Li, L.; Yu, H.; Wang, G.; Weng, H.; Zhang, H.; et al. A Wide-Range Photosensitive Weyl Semimetal Single Crystal-TaAs. *Adv. Mater.* **2018**, *30*, 1801372. [CrossRef]
7. Shekhar, C.; Nayak, A.K.; Sun, Y.; Schmidt, M.; Nicklas, M.; Leermakers, I.; Zeitler, U.; Skourski, Y.; Wosnitza, J.; Liu, Z.; et al. Extremely large magnetoresistance and ultrahigh mobility in the topological Weyl semimetal candidate NbP. *Nat. Phys.* **2015**, *11*, 645–649. [CrossRef]

8. Yuan, X.; Yan, Z.; Song, C.; Zhang, M.; Li, Z.; Zhang, C.; Liu, Y.; Wang, W.; Zhao, M.; Lin, Z.; et al. Chiral Landau levels in Weyl semimetal NbAs with multiple topological carriers. *Nat. Commun.* **2018**, *9*, 1854. [CrossRef]
9. Osterhoudt, G.B.; Diebel, L.K.; Gray, M.J.; Yang, X.; Stanco, J.; Huang, X.; Shen, B.; Ni, N.; Moll, P.J.W.; Ran, Y.; et al. Colossal mid-infrared bulk photovoltaic effect in a type-I Weyl semimetal. *Nat. Mater.* **2019**, *18*, 471–475. [CrossRef]
10. Guo, C.; Tian, H.F.; Yang, H.X.; Sun, K.; Wei, L.L.; Chen, G.F.; Li, J.Q. Hexagonal Phase Intergrown with the Tetragonal Weyl Semimetal TaAs. *Cryst. Growth Des.* **2017**, *17*, 1747–1751. [CrossRef]
11. Boller, H.; Parthe, E. The Transposition Structure of NbAs and of Similar Monophosphides. *Acta Cryst.* **1963**, *1963. 16*, 1095. [CrossRef]
12. Li, Z.; Chen, H.; Jin, S.; Gan, D.; Wang, W.; Guo, L. Chen, X. Weyl Semimetal TaAs: Crystal Growth, Morphology, and Thermodynamics. *Cryst. Growth Des.* **2016**, *16*, 1172–1175. [CrossRef]
13. Sapkota, D.; Mukherjee, R.; Mandrus, D. Single Crystal Growth, Resistivity, and Electronic Structure of the Weyl Semimetals NbP and TaP. *Crystals* **2016**, *6*, 160. [CrossRef]
14. Lin, D.Y.; Guo, B.C.; Dai, Z.Y.; Lin, C.F.; Hsu, H.P. PbI_2 Single Crystal Growth and Its Optical Property Study. *Crystals* **2019**, *9*, 589. [CrossRef]
15. Zhu, P.; Li, Y.; Yang, X.; Yang, Y.; Zhang, X.; Lin, X.; Yang, F.; Li, X.; Wang, Z. Synthesis of Superconducting InxSn1−xTe ($0.04 < x < 0.1$) Large Single Crystal by Liquid Transport Method. *Crystals* **2021**, *11*, 474.
16. Panella, J.R.; Trump, B.A.; Marcus, G.G.; McQueen, T.M. Seeded Chemical Vapor Transport Growth of Cu2OSeO3. *Cryst. Growth Des.* **2017**, *17*, 4944–4948. [CrossRef]
17. Selter, S.; Shemerliuk, Y.; Büchner, B.; Aswartham, S. Crystal Growth of the Quasi-2D Quarternary Compound AgCrP2S6 by Chemical Vapor Transport. *Crystals* **2021**, *11*, 500. [CrossRef]
18. Sun, Z.; Liufu, S.; Chen, X.; Chen, L. Enhanced thermoelectric properties of $Bi_{0.5}Sb_{1.5}Te_3$ films by chemical vapor transport process. *ACS Appl Mater Interfaces* **2011**, *3*, 1390–1393. [CrossRef]
19. Saini, G.S.; Calvert, L.D.; Taylor, J.B. Preparation and Characterization of Crystals of MX- and MX_2 -Type of Niobium and Tantalum. *Can. J. Chem.* **1964**, *42*, 630–634. [CrossRef]
20. Zhang, M.D.; Hou, X.Y.; Wang, Q.; Wang, Y.Y.; Zhao, L.X.; Wang, Z.; Gu, Y.D.; Zhang, F.; Xia, T.L.; Ren, Z.A.; et al. Tip-induced superconductivity on the topological semimetals $TaAs_2$ and $NbAs_2$. *Phys. Rev. B* **2020**, *102*, 085139. [CrossRef]
21. Wang, Y.Y.; Yu, Q.H.; Guo, P.J.; Liu, K.; Xia, T.L. Resistivity plateau and extremely large magnetoresistance in $NbAs_2$ and $TaAs_2$. *Phys. Rev. B* **2016**, *94*, 041103(R). [CrossRef]
22. Peramaiyan, G.; Sankar, R.; Muthuselvam, I.P.; Lee, W.L. Anisotropic magnetotransport and extremely large magnetoresistance in $NbAs_2$ single crystals. *Sci. Rep.* **2018**, *8*, 6414. [CrossRef] [PubMed]
23. Greco, S.; Dal Zilio, S.; Bek, A.; Lazzarino, M.; Naumenko, D. Frequency Modulated Raman Spectroscopy. *ACS Photonics* **2017**, *5*, 312–317. [CrossRef]
24. Liu, H.W.; Richard, P.; Song, Z.D.; Zhao, L.X.; Chen, G.F.; Ding, H. Raman study of lattice dynamics in the Weyl semimetal TaAs. *Phys. Rev. B* **2015**, *92*, 064302. [CrossRef]
25. Chiarello, G.; Hofmann, J.; Li, Z.; Fabio, V.; Guo, L.; Chen, X.; Das Sarma, S.; Politano, A. Tunable surface plasmons in Weyl semimetals TaAs and NbAs. *Phys. Rev. B* **2019**, *99*, 121401. [CrossRef]
26. Liu, H.W.; Zhang, G.H.; Richard, P.; Zhao, L.X.; Chen, G.G.; Ding, H. Spatially Resolved X-ray Photoemission Electron Microscopy of Weyl Semimetal NbAs. *Cryst. Growth Des.* **2018**, *18*, 5210–5213. [CrossRef]
27. Bedoya-Pinto, A.; Pandeya, A.K.; Liu, D.; Deniz, H.; Chang, K.; Tan, H.; Han, H.; Jena, J.; Kostanovskiy, I.; Parkin, S.S.P. Realization of Epitaxial NbP and TaP Weyl Semimetal Thin Films. *ACS Nano* **2020**, *14*, 4405–4413. [CrossRef]
28. Fedotov, A.; Shendyukov, V.; Tsybulskaya, L.; Perevoznikov, S.; Dong, M.; Xue, X.; Feng, X.; Sayyed, M.I.; Zubar, T.; Trukhanov, A.; et al. Electrodeposition conditions–dependent crystal structure, morphology and electronic properties of Bi films. *J. Alloy. Compd.* **2021**, *887*, 161451. [CrossRef]
29. Ross, J.S.; Klement, P.; Jones, A.M.; Ghimire, N.J.; Yan, J.; Mandrus, D.G.; Taniguchi, T.; Watanabe, K.; Kitamura, K.; Yao, W.; et al. Electrically tunable excitonic light-emitting diodes based on monolayer WSe_2 p–n junctions. *Nat. Nanotechnol.* **2014**, *9*, 268–272. [CrossRef]
30. Pezeshki, A.; Shokouh, S.H.; Nazari, T.; Oh, K.; Im, S. Electric and Photovoltaic Behavior of a Few-Layer α-$MoTe_2$/MoS_2 Dichalcogenide Heterojunction. *Adv. Mater.* **2016**, *28*, 3216–3222. [CrossRef]
31. Zhang, S.; Guo, S.; Huang, Y.; Zhu, Z.; Cai, B.; Xie, M.; Zhou, W.; Zeng, H. Two-dimensional SiP: An unexplored direct bandgap semiconductor. *2D Mater.* **2016**, *4*, 015030. [CrossRef]
32. Jing, Y.; Ma, Y.; Li, Y.; Heine, T. GeP_3: A Small Indirect Band Gap 2D Crystal with High Carrier Mobility and Strong Interlayer Quantum Confinement. *Nano Lett.* **2017**, *17*, 1833–1838. [CrossRef]